Copper Cobalt Selenide as a High-Efficiency Bifunctional Electrocatalyst for Overall Water Splitting: Combined Experimental and Theoretical Study

Xi Cao[a], Julia E. Medvedeva[b] and Manashi Nath[a*]*

[a]Department of Chemistry, Missouri University of Science and Technology, Rolla, Missouri 65409, United States.

[b]Department of Physics, Missouri University of Science and Technology, Rolla, Missouri 65409, United States.

KEYWORDS (Water splitting, oxygen evolution reaction, electrocatalyst, metal selenide, DFT calculation).

ABSTRACT Non-precious metal-based catalysts for full water splitting are still being sought after by several groups of researchers, owing to their promising practical application in energy conversion devices. In this article, nanostructured $CuCo_2Se_4$ comprising earth-abundant elements have been reported to exhibit superior bifunctional electrocatalytic activity for both oxygen

evolution reaction (OER) and hydrogen evolution reaction (HER) under alkaline conditions. The $CuCo_2Se_4$ electrocatalyst with a spinel structure type requires low overpotential of 320 mV to reach a current density of 50 mA cm^{-2} for OER and 125 mV to achieve 10 mA cm^{-2} for HER, respectively, which is lower than other reported transition metal chalcogenide electrocatalysts based on Co/Cu, and significantly lower than the well-known precious metal oxide catalysts (IrO_x and RuO_x). To understand the origin of high catalytic performance in $CuCo_2Se_4$, density functional theory (DFT) has been utilized to study the structural, electronic, and magnetic properties of bulk $CuCo_2Se_4$ as well as slabs with (100) and (111) surface orientations with and without OH^- adsorption. The theoretical results show that $CuCo_2Se_4$ is in metallic state with a high electrical conductivity which plays a crucial role in the catalytic activity. Comparison between Co and Cu revealed that Co sites exhibits better OER catalytic activity. Importantly, a surface enhancement of the local magnetic moment on the Co atoms is found to be limited to the top layer in the (100) slab, whereas such variation of the local magnetic moment affects all layers of the (111) slab, strongly favoring OH^- adsorption on Co atom at the (111) surface and making the (111) surface more catalytically active. The different surface energies of (111) and (100) surfaces were also observed from DFT studies which will have a pronounced influence on the observed catalytic activity of these surfaces.

INTRODUCTION

In recent years, generation of alternative renewable energy from sustainable resources has been a topic of growing concern due to faster depletion of fossil fuels and related environmental concerns.[1] Among all the available options, hydrogen appears to be the most promising choice as a clean fuel, which can be widely utilized in fuel cells and other energy storage and conversion devices.[2,3] Among all the possible ways to produce hydrogen, water electrolysis ($2H_2O \rightarrow 2H_2 +$

O_2) can be one of the most useful and clean method to generate hydrogen *on-demand* in copious quantities if the efficiency of the process can be improved significantly.[2,3] Water splitting is composed of two half reactions, oxygen evolution reaction (OER, $4OH^- \rightarrow O_2 + 2H_2O + 4e^-$) occurring at the anode, and hydrogen evolution reaction (HER, $2H_2O + 2e^- \rightarrow H_2 + 2OH^-$) happening at the cathode.[4,5,6,7] The effectiveness of water electrolysis is significantly influenced by the efficiency of OER which is a kinetically sluggish process comprising of multistep proton-coupled electron transfers and the formation of O=O bond which requires high overpotential to initiate the process.[8,9,10,11] Practical applications to produce hydrogen through water splitting has been greatly hindered by the slow OER rate; therefore, it is crucial to develop highly efficient OER electrocatalysts in order to reduce the applied overpotential, facilitate the overall process, and hence improve the energy conversion efficiency.[12,13] Most of the conventionally used state-of-the-art OER electrocatalysts are precious metal-based oxides, such as IrO_x and RuO_x.[14,15,16] However, scarcity and high cost of precious metals have significantly limited their large-scale industrial applications. Consequently, there have been extensive efforts devoted to the development of high-efficiency, low-cost transition metal based OER electrocatalysts.[17,18,19,20,21,22] Such efforts have led to the discovery of several first-row transition metal (Mn, Fe, Co, Ni and Cu etc.) oxides and (oxy)hydroxides as efficient OER electrocatalysts.[23,24,25] Besides oxides and hydroxides, selenides have recently emerged as a new class of highly active OER electrocatalysts showing impressive improvements of catalytic activity compared to oxides.[26,27,28,29] In our group, we have extensively investigated the OER electrocatalytic activity of transition metal chalcogenides, especially selenides (such as Ni_3Se_2, $NiSe_2$, Co_7Se_8, Cu_2Se etc.)[30,31,32,33] and tellurides (Ni_3Te_2)[34] and have observed that the catalytic activity increases with decreasing electronegativity of the lattice anion. Because electronegativity of oxygen (3.44) is larger than that of elemental selenium (2.55), this

implies that selenides should be better OER catalysts, owing to an increased covalency of the metal-chalcogen bond compared to metal oxides. The increased bond strength alters electronic band structure, reduces redox potential of the catalytically-active transition-metal site, reduces band gap, and improves electrical conductivity resulting in higher current density.[35] A study reported by K. Xu et.al comparing oxides (e.g. NiO) and selenides (e.g. Ni_3Se_2) also confirmed that selenides have a more intrinsic metallic state than the oxide phase,[36] which facilitates charge transfer on the catalyst surface and formation of the intermediates, thereby having a positive effect on OER. Our previous studies offered further confirmation where it was shown that the catalyst activation step occurs at a lower potential as covalency increases in the metal-chalcogen bond; for example, Ni_3Te_2 shows lower onset potential and overpotential for OER than Ni_3Se_2.[34] All these considerations may possibly explain the improved OER catalytic activity of selenides and tellurides compared to analogous oxide phases. However, in spite of their enhanced activity a primary concern regarding these chalcogenide electrocatalysts is that they themselves are oxidized rather than water under high anodic potential. Hence, extensive post-OER analysis needs to be carried out to ensure catalyst composition and stability. Apart from changing covalency of the lattice anion, doping at the transition metal site may also lead to redistribution of charge density around the catalytically active site. Accordingly, mixed metal selenides have shown more efficient catalytic performance towards OER. Recently, our group and others have reported mixed-metal selenides such as $Ni_xFe_{1-x}Se_2$, $(Fe_{0.48}Co_{0.38}Cu_{0.14})Se$, $(Co_{0.21}Ni_{0.25}Cu_{0.54})_3Se_2$ and $(Ni_{0.25}Fe_{0.68}Co_{0.07})_3Se_4$ to be excellent OER electrocatalysts with low onset potential and increased energy conversion efficiency.[37,38,39,40] Some of these previous studies reported that the oxidized redox couples of the transition metal (e.g. $Co^{3+/4+}$) plays a very crucial role in influencing the catalytic activity.[41,42,43] Specifically, it was suggested that higher *d*-electron occupancy preferably

with one electron in the doubly degenerate e_g orbital significantly improves the catalytic activity.[42] Although catalyst compositions containing Co, Ni, and Fe have been extensively researched for OER activity, Cu which satisfies the *d*-electron occupancy criteria above, has not been investigated extensively for OER catalytic activity until recently.[44,45] Bikkarolla et al. synthesized $CuCo_2O_4$ nanoparticles on nitrogenated graphene and showed an overpotential of 360 mV to reach 10 mA cm^{-2} and high stability in alkaline media.[46] In another report, two-dimensional $CuCo_2S_4$ nanosheets were synthesized by a simple hydrothermal method and showed high OER activity at low mass loading.[47] Addition of Cu to the composition is expected to increase the metallicity in the catalyst composite, thereby, facilitating the charge transfer rate. Hence, the introduction of Cu in the catalyst composition deserves more attention, especially since Cu is one of the most earth-abundant non-precious elements. Apart from the chemical composition of the catalyst site, crystal structure and coordination geometry also play a subtle role in influencing the catalytic activity. Accordingly, spinel type compounds containing mixed valence metal ions in variable coordination geometries have attracted a lot of attention in that respect since they are believed to have high OER activity at the trivalent metal sites facilitating charge transfer rates between the reactant species or intermediates and the catalyst surface.[13,48]

In this article, we have reported high-efficiency bifunctional electrocatalytic activity of $CuCo_2Se_4$ nanoparticles for OER and HER in harsh alkaline medium. The catalyst composite exhibits a low onset potential of 1.43 V vs RHE and an overpotential of 320 mV to achieve 50 mA cm^{-2} for OER in alkaline solution, which is one of the lowest overpotentials that has been reported till date. Moreover, the catalyst also shows excellent HER activity with a low overpotential of 125 mV (at 10 mA cm^{-2}) in alkaline medium. A full water electrolysis cell comprising $CuCo_2Se_4$ nanoparticles modified electrode as both OER and HER catalysts required a cell voltage of only

1.782 V to drive a current density of 50 mA cm^{-2} for the overall water splitting. We have also employed density functional theory (DFT) to study electronic band structure of $CuCo_2Se_4$ and to correlate the results with observed high OER catalytic activity. The calculated electronic and magnetic properties of bulk $CuCo_2Se_4$ were compared with those for slabs with (100) and (111) lattice orientations, to investigate surface dependent catalytic activity. These calculations suggests that $CuCo_2Se_4$ is in the metallic state with high electrical conductivity. The (100) slab has a low surface energy ($E_{surface}$) of 136 meV/f.u., suggesting it is likely to be the most thermodynamically stable surface orientation, while the (111) slab with a higher $E_{surface}$, 243 meV/f.u., and intense metallic nature near the Fermi level is expected to be the most active surface for OER .[49] We have also estimated and compared OH^- adsorption energy on Co and Cu sites in the (100) and (111) lattice planes, and observed that while both Cu and Co atoms play a crucial role as the catalytically active sites, Co atom is a more favorable active site since the adsorption energy of OH^- on Co is 531 meV higher than that on Cu atom (at 100 surface), suggesting OH^- prefers to bond to Co atom instead of Cu on the surface.

EXPERIMENTAL AND COMPUTATIONAL METHODS

Chemicals and Materials. All chemicals were of analytical grade and used without further purification. Distilled water (18 MΩ/cm) was used to prepare all the solutions. Cobalt chloride hexahydrate [$CoCl_2 \cdot 6H_2O$] was purchased from J. T. Baker Chemical Co., copper chloride dihydrate [$CuCl_2 \cdot 2H_2O$] and potassium hydroxide [KOH] from Fisher Scientific, selenium dioxide [SeO_2] and hydrazine monohydrate [$N_2H_4 \cdot H_2O$] from Acros chemicals. Carbon fiber paper (CFP) and Au-coated glass used as conductive substrates were purchased from FuelCellsEtc, Texas and Deposition Research Lab Incorporated (DRLI), Lebanon Missouri, respectively. All Au coated

glass substrates were carefully cleaned by treatments in Micro-90, isopropanol and deionized (DI) water while CFP were cleaned by simply soaking into isopropanol.

Synthesis of $CuCo_2Se_4$. In a typical synthesis of $CuCo_2Se_4$ by hydrothermal method, 10 mM of $CuCl_2 \cdot 2H_2O$, 20 mM of $CoCl_2 \cdot 6H_2O$ and 40 mM of SeO_2 were mixed in 10 mL of deionized water, then the mixture was stirred on a magnetic stirrer to form a homogenous solution. After 10 min of stirring, 0.5 mL of hydrazine ($N_2H_4 \cdot H_2O$) was added carefully and then a brown colloidal solution was formed. The resulting solution was stirred for another 10 min and then transferred into a 23 mL Teflon-lined stainless-steel autoclave. The autoclave was tightly sealed and maintained at 145 °C for 24 h and then naturally cooled down to room temperature. The final blackish product was collected by means of centrifugation, followed by washing several times with distilled water and absolute ethanol. The product was dried in the vacuum oven at room temperature for overnight.

Electrode Preparation. To prepare the catalyst ink, 2.0 mg $CuCo_2Se_4$ nanoparticles were dispersed into 1.0 mL 0.8 % Nafion® ethanol solution, followed by 30 min ultrasonication. Both Au coated glass and CFP substrates were covered with a Teflon tape, leaving an exposed geometric area of 0.070 cm^2 on which 20 μL of the homogeneous catalyst ink was drop-casted. The electrodes with a loading of ~ 0.57 mg cm^{-2} were dried at room temperature. After being heated at a constant temperature of 130 °C for 30 min in a vacuum oven, the electrodes were ready for electrocatalytic measurements.

Characterization. The catalyst composite was characterized through powder X-ray diffraction (PXRD) using Philips X-Pert X-ray diffractometer (PANalytical, Almelo, The Netherlands) with a Cu Kα (1.5418 Å) radiation. Morphology of the product was observed with a scanning electron microscope (SEM, Hitachi S4700) using an acceleration voltage of 15 kV and a working distance

of 12 mm. Energy dispersive spectroscopy (EDS) was also obtained from the same SEM to identify relative atomic ratio of the constituent elements in the catalyst composite. X-ray photoelectron spectroscopy (XPS) of the catalyst before and after catalytic activity was carried out using a KRATOS AXIS 165 X-ray Photoelectron Spectrometer with the monochromatic Al X-ray source. All XPS analysis was performed on the pristine catalyst surface without any sputtering.

Electrochemical measurements. The electrocatalytic performances of $CuCo_2Se_4$ were investigated in 1.0 M KOH solution at room temperature in a three-electrode system by an IviumStat potentiostat. The OER and HER catalytic activities were studied from linear scan voltammetry (LSV) while the stability of the catalyst was estimated by chronoamperometry at a constant applied potential. A three-electrode cell comprising $CuCo_2Se_4$ drop-casted on various substrates (Au coated glass or CFP) serving as the working electrode, glassy carbon (GC) as the counter electrode and an Ag|AgCl (KCl saturated) reference as the reference electrode was used for all electrochemical measurements. All measured potentials vs Ag|AgCl (KCl saturated) were converted to the reversible hydrogen electrode (RHE) according to the Nernst equation (eq. 1).

$$E_{RHE} = E_{Ag|AgCl} + 0.059pH + E^{\circ}_{Ag|AgCl} \quad (1)$$

Where E_{RHE} is the calculated potential vs RHE, and $E^{\circ}_{Ag|AgCl}$ is the standard thermodynamic potential of Ag|AgCl (KCl saturated) at 25.1 °C (0.197 V), and $E_{Ag|AgCl}$ is the experimentally measured potential vs Ag|AgCl (KCl saturated) reference electrode.

Density Functional Theory Calculations. The electronic properties of $CuCo_2Se_4$ in bulk and slab geometries were studied using first-principles density functional calculations as implemented in the Vienna ab initio simulation package (VASP).[50,51,52,53] The generalized gradient

approximation in the Perdew-Burke-Ernzerhof (PBE) form,[54] within the projector augmented-wave method was used.[55,56] The generalized gradient approximation with an on-site Coulomb U term (GGA+U) method has been shown to successfully describe the cohesive energy, electronic structure, and mechanical and magnetic properties of bulk and surfaces of 3*d*-metal based materials.[57,58] In this work, GGA+U method,[59] with U = 0 and 6 eV for Co-*d* states and U = 0 and 4 eV for Cu-*d* states was used to study the electronic structure and magnetic properties of bulk and slabs of $CuCo_2Se_4$ as well as the adsorption energy of OH^- at the surfaces. Moreover, it allowed for straightforward comparisons with previous reports. The internal atomic positions for all structures were optimized using force and total energy minimization until the Hellmann-Feynman force on each atom was below 0.01 eV/Å. Brillouin-zone sampling was done with Γ-centered Monkhorst-pack with k-mesh of at least 4x4x4; the cut-off energy of 500 eV was used for bulk and slab geometries.

Results and Discussion

Figure 1a shows the pxrd pattern of the as-synthesized $CuCo_2Se_4$ which exhibits a close similarity with the standard $CuCo_2Se_4$ pattern (PDF # 04-019-0997). A trace amount of $Cu_{2-x}Se$ (PDF # 00-027-1131) could also be detected in the pxrd pattern. Approximate size of the crystalline domains was calculated from line broadening of the diffraction peaks to be approximately 2.67 nm using the Scherrer equation.[60] Interestingly, $CuCo_2Se_4$ belongs to a spinel structure type, AB_2X_4, (*X* = chalcogen atom). Among the metals *A* and *B*, *A* is a divalent cation occupying the partially occupied tetrahedral layer, while *B* is a trivalent cation occupying the fully occupied octahedral metal layer. From the crystal structure illustration (inset of Figure 1a), it was observed that there is only one type of Co/Cu atom, and the bond lengths of Co-Se and Cu-Se are ~ 2.385 and 2.378

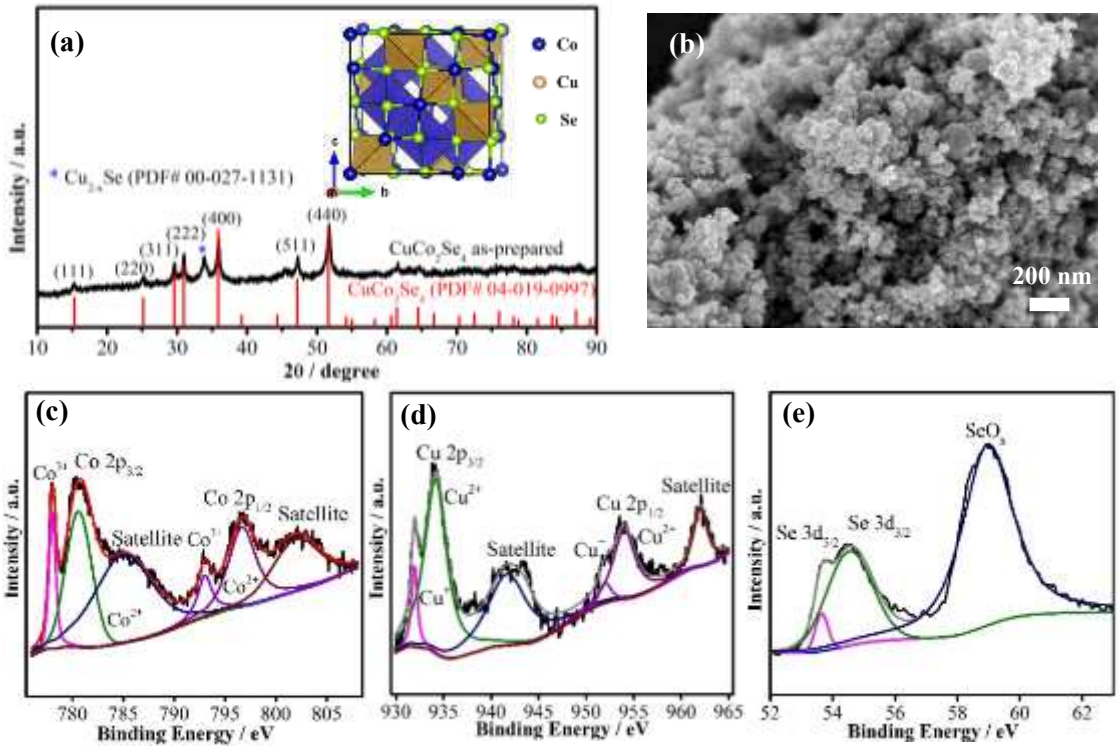

Figure 1. (a) PXRD pattern of the as-synthesized $CuCo_2Se_4$ nanoparticles. The inset of (a) shows the crystal structure of $CuCo_2Se_4$ created from the cif file corresponding to PDF # 04-019-0997. (b) SEM image of the as-synthesized $CuCo_2Se_4$. Deconvoluted XPS spectra of (c) Co 2p, (d) Cu 2p and (e) Se 3d collected from the as-synthesized catalyst.

Å, respectively. Cu atoms predominantly occupied the tetrahedral sites, while Co atoms were in the octahedral coordination sites.

SEM images of as-synthesized $CuCo_2Se_4$ catalyst showed small granular and nanocoral-like morphology with wide size distribution (20 – 200 nm) as shown in Figure 1b. Such nanostructured geometries are highly advantageous for catalytic applications since they provide high active surface area. The chemical composition and oxidation states of as-prepared $CuCo_2Se_4$ catalyst were further determined by X-ray photoelectron spectroscopy (XPS)

shown in Figure 1c-e. It should be mentioned that all binding energies of Co, Cu and Se were calibrated with respect to a reference binding energy of C 1s (284.5 eV). Co 2p XPS peaks were observed at 777.8 and 793.3 eV confirming the presence of Co-selenide phases.[31] Similarly the Cu 2p XPS peaks observed at 933.8 and 954.1 eV confirmed the presence of copper-selenide linkages.[32] The oxidation states of Cu, Co and Se in as prepared catalyst were further evaluated from the deconvoluted XPS spectra presented in Figure 1c-e. The deconvoluted Co 2p and Cu 2p spectra confirmed presence of mixed oxidation states of Co^{2+}/Co^{3+} and Cu^{+}/Cu^{2+}, respectively. The Co 2p XPS spectrum in Figure 1c could be deconvoluted to reveal peaks at 780.5 and 796.8 eV corresponding to Co^{2+} $2p_{3/2}$ and Co^{2+} $2p_{1/2}$; while peaks at 777.8 and 793.3 eV correspond to Co^{3+} $2p_{3/2}$ and Co^{3+} $2p_{1/2}$, respectively.[61] The obvious satellite peaks of Co 2p can be found at 785.5 and 802.2 eV.[85] Similarly, in the Cu 2p deconvoluted spectra (Figure 1d), peaks at 931.5 and 952.5 eV correspond to Cu^{+} $2p_{3/2}$ and Cu^{+} $2p_{1/2}$ while those at 933.8 and 954.1 eV were assigned to Cu^{2+} $2p_{3/2}$ and Cu^{2+} $2p_{1/2}$ with its shake-up satellite peaks at 941.8 and 961.7 eV.[47] In the Se 3d spectra (Figure 1e), the peaks at 54.0 and 54.9 eV correspond to Se $3d_{5/2}$ and Se $3d_{3/2}$, respectively, which confirm the presence of Se^{2-}.[31] The peak at ≈ 59 eV indicates the existence of SeO_x species which might due to the surface oxidation of selenide. However, no metal oxides were detected on the catalyst surface from XPS analysis. It was found that the cations in the as-prepared catalyst contained 8 % of Co^{3+}, 45 % of Co^{2+}, 9 % of Cu^{+} and 38 % of Cu^{2+}.

To measure the electrocatalytic performances, $CuCo_2Se_4$ nanoparticles were drop-casted on Au coated glass following standard procedures as described above. Linear sweep voltammetry (LSV) was performed to measure all the catalytic activities in alkaline solution (1.0 M KOH), while the catalyst durability was studied through chronoamperometry measurements by applying a constant voltage. The electrochemically active surface area (ECSA) as shown in Figure S1 was estimated

by measuring the double layer charging current in non-Faradaic region at different scan rates following reported procedure.[9] The anodic and cathodic capacitive current (i_{DL}) at 0.01 V vs Ag|AgCl (KCl saturated) was plotted as a function of scan rate (v) as shown in Figure S1 (insert), and the value of C_{DL} can be obtained from the average of anodic and cathodic slopes according to eq. 2. The ECSA of $CuCo_2Se_4$ catalyst was calcuated from eq. 3 while the roughness factor (RF) was estimated from the ratio of ECSA and the geometric area (0.07 cm^2).

$$i_{DL} = C_{DL} \cdot \nu \tag{2}$$

$$ECSA = \frac{C_{DL}}{C_S} \tag{3}$$

C_{DL} is the double layer capacitance and C_S is the specific capacitance of the electrocatalyst per unit area measured in similar electrolyte. In this study, C_S was taken as 0.040 mF cm^{-2} based on reported values.[9] As can be seen in Figure S1(a) and Table S1, ECSA of the catalyst was estimated to be 5.325 cm^2 and RF was calculated as 76.07, confirming that the active surface of these

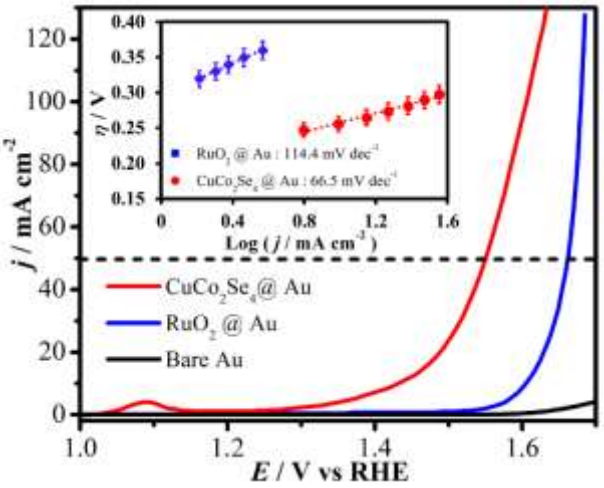

Figure 2. Polarization curves of $CuCo_2Se_4$@Au, RuO_2@Au and bare Au substrate in N_2-saturated 1.0 M KOH at a scan rate of 10 mV s^{-1}. The inset shows Tafel plots of $CuCo_2Se_4$@Au and RuO_2@Au with errors bars as marked.

nanostructured catalysts was indeed highly rough. It is well known that the catalytic activity is expected to be improved by rough catalyst surface due to more extensive exposure of catalytically active sites to the electrolyte.

For comparison of the electrocatalytic performance of $CuCo_2Se_4$ with known standards, state-of-the-art OER catalyst RuO_2@Au with a similar loading was also prepared in our laboratory by electrodeposition following a typical procedure described in supplementary information,[62] and its catalytic activity was measured under the exact same condition. Figure 2 shows the OER polarization curves of $CuCo_2Se_4$@Au-glass, RuO_2@Au-glass and bare Au-coated glass measured in N_2-saturated 1.0 M KOH at a scan rate of 10 mV s^{-1}. As expected, negligible catalytic activity was obtained on bare Au-coated glass while $CuCo_2Se_4$@Au was highly active towards OER and exhibited efficient oxygen evolution activity with a very low onset potential of 1.43 V *vs* RHE as shown in Figure 2 and in the magnified plots shown in Figure S2. The current density of $CuCo_2Se_4$ increased very rapidly after onset and it yielded a current density of 50 mA cm^{-2} at an overpotential of only 320 mV, which was much better compared to the state-of-the-art RuO_2 (430 mV at 50 mA cm^{-2}). The catalyst loading in this work was 0.57 mg cm^{-2} and the gravimetric current density corresponding to mass activity of $CuCo_2Se_4$ have been shown in Figure S3, which requires an overpotential of 280 mV to reach 50 mA mg^{-1}. Turnover frequency (TOF) is an important parameter to evaluate a catalyst performance. The TOF was estimated using standard procedure as mentioned in the supporting information. As seen in the Figure S4, TOF of $CuCo_2Se_4$ was estimated to be 0.00121 s^{-1} and 0.041 s^{-1} at onset potential and η = 300 mV, respectively, which are much higher than RuO_2 indicating superior catalytic performance of $CuCo_2Se_4$ towards OER. The exchange current density (j_0) of $CuCo_2Se_4$ and RuO_2 estimated from the Tafel plots (inset of

Figure 2) are 0.0138 mA cm^{-2} and 0.00598 mA cm^{-2} respectively, demonstrating $CuCo_2Se_4$ is indeed more efficient OER electrocatalyst. In order to investigate the effect of substrates, OER activity of $CuCo_2Se_4$ catalyst also studied on different substrates (Au-coated glass and carbon fiber paper) as shown in Figure S5. $CuCo_2Se_4$ exhibited almost similar activities on both the substrates, which meant the catalyst itself was intrinsically very efficient for OER independent of 2D flat or 3D porous substrates. The catalytic activity of $CuCo_2Se_4$ was also compared with binary metal selenides, Cu_3Se_2, Cu_2Se, Co_7Se_8 and CoSe (shown in Figure S6) to understand the influence of transition metal doping in the catalytic site as well as influence of crystal structure. As can be seen clearly, the mixed metal selenide was more active than any of the binary Co or Cu-based selenides. Moreover, ECSA of Cu_2Se and CoSe with same loading as $CuCo_2Se_4$ was also measured under the same condition as $CuCo_2Se_4$. As can be seen in Figure S1 and Table S1, both Cu_2Se and CoSe showed higher ECSA and RF in comparison to $CuCo_2Se_4$ which further confirms that the enhancement in OER efficiency is due to the superior intrinsic catalytic activity of mixed metal electrocatalyst. Tafel slope is another important kinetic parameter to explain the high catalytic performance of $CuCo_2Se_4$, which showed a modest slope of 66.5 mV $decade^{-1}$ (inset of Figure 2), indicating OER on $CuCo_2Se_4$ surface was kinetically favorable.

To further understand the high OER activity of $CuCo_2Se_4$ catalyst, electrochemical impedance spectroscopy (EIS) was performed to estimate internal resistance of the catalyst composite as well as charge-transfer resistance at the catalyst (electrode)-electrolyte interface. The Nyquist plot of $CuCo_2Se_4$ catalyst was obtained at an applied potential of 1.45 V vs RHE in N_2-saturated 1.0 M KOH solution as shown in Figure 3. The electrolyte resistance (R_s), resistance of the catalytic composite ($R_{catalyst}$), and charge transfer resistance (R_{ct}) can be obtained from the equivalent circuit as fitted from the Nyquist plot of $CuCo_2Se_4$ catalyst (insert in Figure 3), and the values obtained

from the fit have been listed in Table 1. As can be seen, the uncompensated electrolyte resistance R_s was obtained as 5.0 Ω, which was subsequently used for iR correction. From the fitting of the equivalent circuit it was estimated that R_{ct} and $R_{catalyst}$ of catalyst composite was 9.34 and 716.6 Ω, respectively. The charge transfer resistance derived from lower frequency region was closely related to the kinetics the OER process on the catalyst surface. Hence, the smaller the value of R_{ct} indicates a more efficient electron transfer at the catalyst-electrolyte interface leading to faster OER reaction rate and subsequently showing better catalytic activity consistent with the low overpotential obtained from electrocatalytic measurements as reported above. Lower catalyst resistance ($R_{catalyst}$) on the other hand, leads to better charge transport within the catalyst composite resulting in faster kinetics and higher current density at low potentials .[63]

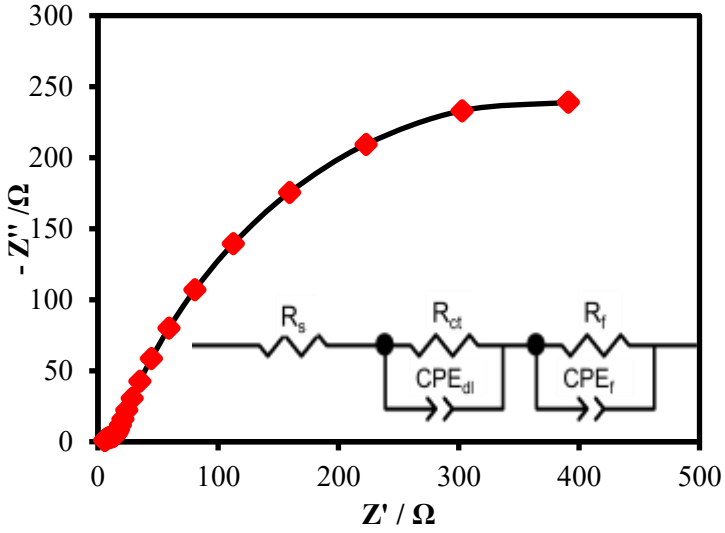

Figure 3. Nyquist plot obtained from EIS measurements of the $CuCo_2Se_4$ catalyst at applied potential of 1.45 V vs RHE in N_2-saturated 1.0 M KOH solution. Symbols indicate the raw data, while solid lines represent the corresponding fit to equivalent circuit model. Inset shows the equivalent circuit of catalysts. R_s is the resistance of the electrolyte; R_{ct} is the electron transfer resistance; CPE_{dl} is the constant phase element of double-layer nonideal capacitance; $R_{catalyst}$ is resistance of the catalyst layer; and $CPE_{catalyst}$ is the capacitance.

The OER Faradaic efficiency of $CuCo_2Se_4$ catalyst was evaluated by water-displacement method, wherein, the volume of the gas evolved was directly measured employing methods as has been described previously.[34] The theoretical amount of evolved O_2 was estimated from the anodic current and was compared with the experimentally measured volume of O_2. A Faradaic efficiency of nearly 100% was obtained for $CuCo_2Se_4$ catalyst toward OER reaction.

Table 1. Equivalent Circuit Parameters Obtained from Fitting of EIS Experimental Data.

Parameters	Value
R_s/Ω	5.0
R_{ct}/Ω	9.34
CPE_{dl}/F	0.63
$R_{catalyst}/\Omega$	716.6
$CPE_{catalyst}/F$	0.75

The durability of an electrocatalyst for continuous oxygen evolution under operational conditions is a crucial factor to evaluate its practical application. Chronoamperometric measurement, at a constant applied potential of 1.47 V vs RHE to achieve a current density of around 8.0 mA cm^{-2}, was used to investigate stability of $CuCo_2Se_4$ catalyst for 8 h (shown in Figure 4a insert). As can be seen, current density slightly increased after 8 h aging in alkaline medium indicating an increase of catalytic activity. Such increase of catalytic activity has been previously observed in Nafion®-containing catalytic films and can be explained by increasing porosity of the Nafion® composite as O_2 is evolved during continuous OER. Figure 4a shows the comparison of LSV polarization curves before and after 8 h of chronoamperometry in 1.0 M KOH indicating excellent stability of the catalyst under conditions of continuous O_2 evolution with improved activity after 8 h. To confirm the compositional stability, crystalline structure of $CuCo_2Se_4$ after 8 h of chronoamperometry was studied by pxrd which indicated presence of only $CuCo_2Se_4$ as the major crystalline phase without any other metal oxides or hydroxides as shown in Figure 4b.

Morphology of the catalyst after 8 h chronoamperometry was investigated by SEM as shown in Figure S7, which showed that the catalyst had similar morphologies before and after prolonged catalytic activity. XPS spectra collected after chronoamperometry demonstrated that the peaks of Co 2p, Cu 2p and Se 3d (shown in Figure 4c-e) remain unchanged in terms of peak position. A comparison of the XPS peaks of pristine $CuCo_2Se_4$ and the sample after 8 h chronoamperometry as shown in Figure S8 also revealed the close similarity of the peaks indicating no change in surface composition. The O 1s spectra was also measured as shown in Figure S8 (d) before and after 8h of chronoamperometry, which interestingly, still did not show any evidence of metal oxides, but indicated the presence of only surface adsorbed oxygen species and trace amounts of SeO_2 after 8 h of chronoamperometry. The XPS spectra as shown in Figure 4c-e was deconvoluted to analyze different oxidation states of the elements revealing that the cations after 8 h of aging the catalyst included 14 % of Co^{3+}, 38 % of Co^{2+}, 9 % Cu^{+} and 39 % of Cu^{2+}. It is interesting to observe that the sample after chronoamperometry contained similar percentage of Cu^{+} and Cu^{2+}, while the amount of Co^{3+} increased by 6 % and Co^{2+} decreased by 7 % in comparison with the as-prepared $CuCo_2Se_4$. The $CuCo_2Se_4$ catalyst after 8 h chronoamperometry was also studied by EDS which confirmed that the atomic ratio of Cu, Co and Se before and after chronoamperometry were almost same (relative atomic percentages have been listed in Table S2 in supporting information). All these post-OER activity and compositional analysis revealed that the catalyst was indeed stable in corrosive alkaline conditions under long-term exposure. Based on structural characterization and spectral analysis, it is believed that the catalyst surface will form a partially hydroxylated

mixed anionic (hydroxy)selenide (better represented as *M*(OH)Se) surface in alkaline medium retaining its selenide coordination.

$CuCo_2Se_4$ nanoparticles also exhibited remarkable electrocatalytic activity for hydrogen evolution reaction (HER) at the cathode in N_2-saturated 1.0 M KOH. Polarization curves of $CuCo_2Se_4$@Au-glass were measured with a scan rate of 10 mV s^{-1} and compared with Pt mesh under the same condition shown in Figure 5. It can be seen that an overpotential of 125 and 232 mV for $CuCo_2Se_4$ was required to achieve a cathodic current density of 10 and 50 mA cm^{-2},

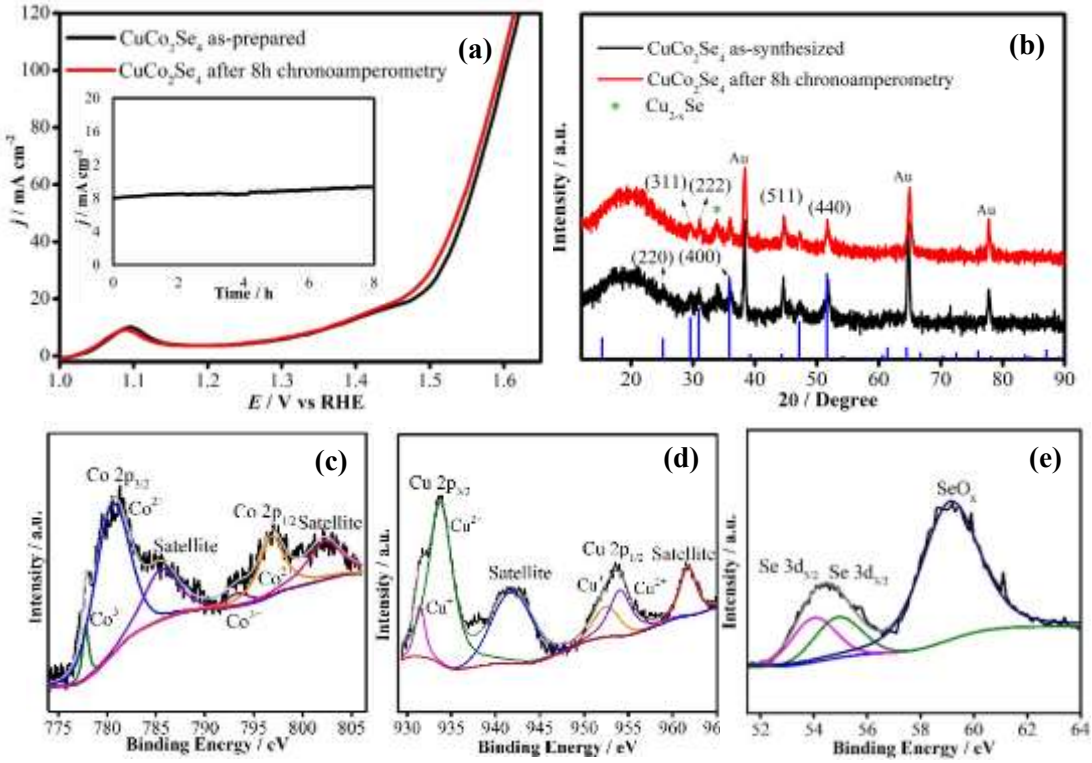

Figure 4. (a) Comparison of LSV curves of $CuCo_2Se_4$ catalyst measured in N_2-saturated 1.0 M KOH before and after 8 h chronoamperometry. The inset shows chronoamperometric measurement of $CuCo_2Se_4$ under continuous O_2 evolution. (b) Comparison of pxrd of $CuCo_2Se_4$ on Au substrate before and after 8 h chronoamperometry. XPS spectra of (c) Co 2p, (d) Cu 2p and (e) Se 3d after chronoamperometric measurement for 8 h.

respectively, which was just slightly higher than that of Pt.[64] With a very low onset potential of -47 mV vs RHE obtained from the magnified LSV plot shown in Figure S9, the cathodic current density of $CuCo_2Se_4$ catalyst increased rapidly indicating excellent conductivity of the catalyst. Stability of the catalyst for continuous H_2 evolution was measured at -0.11 V vs RHE to achieve a cathodic current density around -7 mA cm^{-2} in 1.0 M KOH for 4.5 h as shown in the inset of Figure 5. As can be seen, the current density was similar before and after 4.5 h aging. The LSVs before and after chronoamperometry have been compared in Figure 5 which shows almost same behavior towards HER further confirming the stability of $CuCo_2Se_4$ as HER catalyst in alkaline medium. TOF is also very important parameter to evaluate the performance of HER electrocatalyst. As can be seen in Figure S10, the TOF values of $CuCo_2Se_4$ for HER process are 0.000174 s^{-1} and 0.007 s^{-1} at onset potential and η = 100 mV respectively.

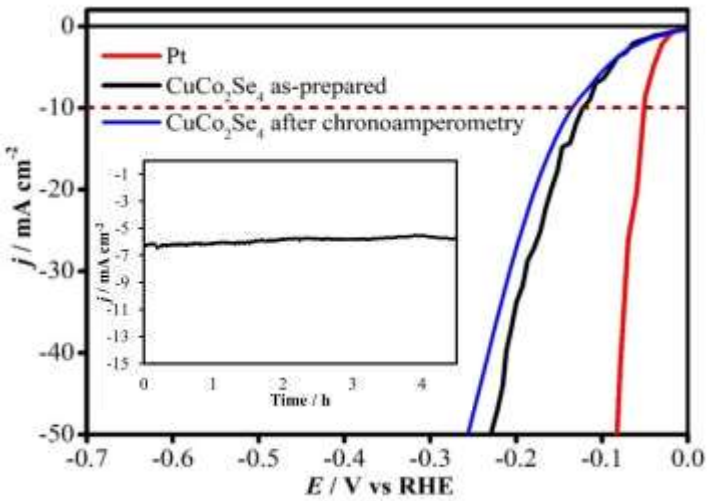

Figure 5. HER activity of $CuCo_2Se_4$@Au measured in N_2-saturated 1.0 M KOH at a scan rate of 10 mV s^{-1} compared with that of Pt mesh. The plot also shows the polarization curve after chronoamperometry. Inset shows the chronoamperometric study of $CuCo_2Se_4$@Au for 4.5 h of continuous H_2 evolution.

Since $CuCo_2Se_4$@Au exhibited highly efficient bifunctional electrocatalytic activity for both OER and HER in alkaline medium, so an electrolyzer was made using $CuCo_2Se_4$@Au-glass electrodes as both cathode and anode for full water splitting at room temperature (Figure S11). $CuCo_2Se_4$@Au||Pt and RuO_2||Pt couples were also measured in N_2-saturated 1.0 M KOH solution and compared with $CuCo_2Se_4$@Au||$CuCo_2Se_4$@Au as shown in Figure S12. As expected, combining $CuCo_2Se_4$@Au anode and Pt cathode exhibited the highest efficiency while the RuO_2||Pt couple produced diminished catalytic activity. $CuCo_2Se_4$@Au||$CuCo_2Se_4$@Au electrolyzer required a cell voltage of 1.782 V to reach a current density of 50 mA cm^{-2} shown in Table S3.

To better understand the effects of electronic properties of $CuCo_2Se_4$ on its outstanding OER catalytic activities, DFT calculations were performed to evaluate the electronic band structure for bulk $CuCo_2Se_4$, slab with (100) terminated surface, and slab with (111) surfaces with Co/Cu termination and Co-only termination, as shown in Figure 6. All the crystal structures for bulk and slabs of $CuCo_2Se_4$ (Figure 6) were plotted using VESTA software.[65] The corresponding supercells

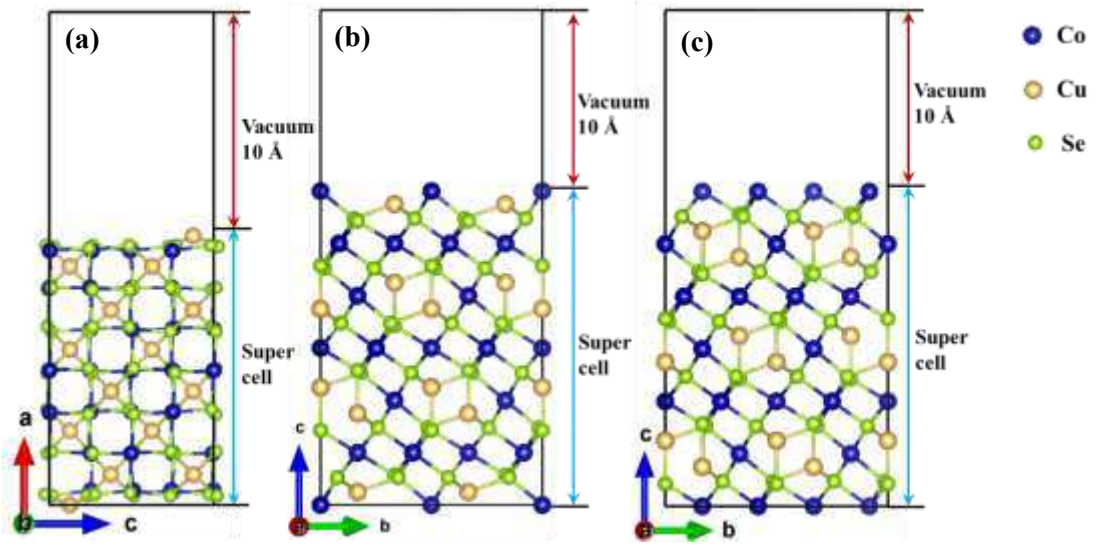

Figure 6. Slab supercells for (100) surface (a), (111) surface with Cu/Co termination (b) and (111) surface with Co-only termination (c). Color coded: navy – Co, yellow – Cu, green – Se.

are $Cu_8Co_{16}Se_{32}$ (4 formula units, f.u.) as shown in Figure 6 (a), $Cu_{14}Co_{28}Se_{56}$ (7 f.u.) in Figure 6 (b), and $Cu_{24}Co_{48}Se_{96}$ (12 f.u.) in Figure 6 (c), respectively. To study surface properties in the 2D structures under periodic boundary conditions, a relatively large vacuum layer of around 10 Å was used to separate the 2x2 slabs in order to avoid interaction between them. The slab thickness is about 17 Å for both the (100) and (111) surfaces that corresponds to seven Co-containing layers.

The total density of states (DOS) and partial density of states (PDOS) of bulk $CuCo_2Se_4$ calculated using GGA+U with U = 6 eV for Co *d*-states and U = 4 eV for Cu *d*-states are presented as solid lines in Figure S13. The valence band (VB) mainly consists of the *d*-orbitals from Co and Cu hybridized with the *p*-orbitals of Se, while the conduction band (CB) is mainly composed of both the empty *d*-orbitals in Co and the antibonding *p*-orbitals of Se. This result suggests the occurrence of *d*-*d* transitions between Co and Cu, and the charge transfer between metal and Se. Importantly, the continuous distribution of DOS near the Fermi level indicates that $CuCo_2Se_4$ is in metallic state with high electrical conductivity,[40] resulting from the PDOS contribution of Co and Se atoms as shown in Figure S13 (c) and (d). This result is also consistent with the electrochemical impedance spectra (EIS) measurement shown in Figure 3 and Table 1 which revealed that $CuCo_2Se_4$ catalyst has a relatively low catalyst resistance as well as charge transfer resistance, therefore facilitates fast electron transport during the electrocatalytic process.[44] The DOS and PDOS plots calculated using GGA method are also given as dashed lines in Figure S13 for comparison. Most importantly, GGA or GGA+U with U=5 eV or smaller result in a non-magnetic solution, whereas the magnetic moment of 0.79 μ_B on Co atoms was obtained for U=6 eV. For the latter case, there is a significant effect of U_{eff} on the occupied Co 3*d* states than on Cu 3*d* states in VB; the changes in CB are caused primarily by the magnetic interactions on Co atoms that push the spin-down empty 3*d*-states of Co to a higher energy.

In Figure 7, the total density of states (TDOS) of bulk $CuCo_2Se_4$, (100) slab, (111) slab with Co/Cu and (111) only-Co terminated planes, all calculated within GGA+U, have been compared. It can be noticed that bulk and both (100) and (111) surfaces are in the metallic state. The (100) surface shown in Figure 7 (b) exhibits a similar TDOS in the vicinity of the Fermi level as that of bulk $CuCo_2Se_4$, while (111) surface as shown in Figure 7 (c) and (d) show a more intense TDOS near the Fermi level; thus, suggesting a higher electronic conductivity. It is also interesting to observe the trend that from bulk to (100), (111) Co/Cu and (111) Co surfaces width of the CB narrows, effectively shifting top of the CB around 2 eV toward the Fermi level. Such shift indicates that the (111) surface has more metallic character and the *d*-*d* localization might take place among Cu and Co atoms. During OER process, active sites can be stabilized by charge transfer that enhances the efficiency of absorbing intermediate species, which has been widely agreed upon as being one of the important factors to affect the OER catalytic activity.[66,67] Hence, it is reasonable to conclude that the (111) surface with Co-terminated lattice plane is more catalytic favorable than (111) Co/Cu and (100) plane or even bulk. Based on the calculated surface Gibbs free energy, the $E_{surface}$ is 136 meV for (100), 280 meV for (111) Co/Cu, and 242 meV for (111) Co-terminated surface. Hence, the thermodynamic stability of surfaces orientations is as follows: (100) > (111) Co > (111) Co/Cu, indicating that the (100) surface should be more thermodynamically favorable. For the (111) surface, termination with Co layer is more stable than that with Co/Cu, so it is easier to form (111) Co termination under directional growth. It is important to stress that the thermodynamically stable lattice plane will not necessary have more metallic states to reduce the overpotential: In fact, Yagi group has reported that the surface with higher energy can lead to a higher adsorption energy of hydroxide species to facilitate the catalytic activity.[68] In another report, Wang's group has also studied Co_3O_4 nanocrystals exposed with different lattice planes and

showed that (111) is the most catalytically active plane with the highest $E_{surface}$.[69] Indeed, a surface with higher energy is expected to have structural defects that attract hydroxide species as adsorbents to reduce the surface energy. Hence in this work, we focused on the comparison between the (100) and (111) Co/Cu terminated planes and investigated the OH^- absorption on Co and Cu sites for both surface orientations.

To further analyze the electronic properties of (100) and (111) surfaces, the DOS of top layer in (100) and (111) Co/Cu, the PDOS of a single Co atom located in the top surface layer (layer 0) and in the center layer (layer 3, close to the bulk property) have been plotted and compared as shown in Figure S14. As can be seen in Figure S14 (a), the Co atom in the surface layer contributes at the bottom of VB in the (100) case, i.e., shifted by almost 3 eV toward a more negative energy as compared to the Co atom in the center layer. In marked contrast, the energy position of the Co VB states remains almost same in the (111) Co/Cu case shown in Figure S14 (b). Hence, in the

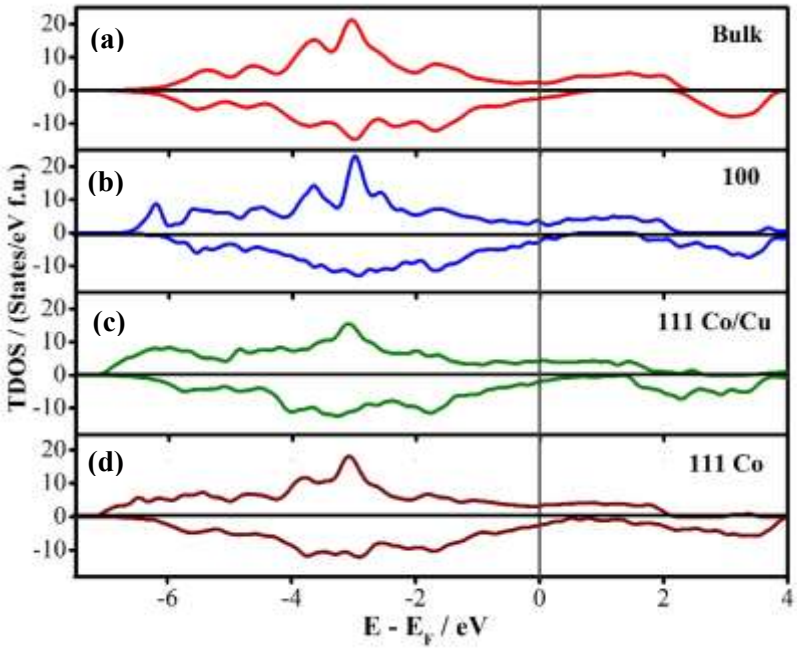

Figure 7. Total density of states (TDOS) of bulk $CuCo_2Se_4$ (a), (100) surface (b), (111) surface with Co/Cu (c) and Co (d) termination.

(100) case, the electronic properties of the surface top layer deviate significantly from those in bulk – in accord with the variation of the Co magnetic moments given in Table S4, whereas the changes occur even in the center layer for the (111) Co/Cu slab. For the Co atom located in the surface layer, the VB of both (100) and (111) Co/Cu are similar, while the CB in (111) is slightly closer to the Fermi level.

To understand the differences in electronic and magnetic properties of the top layer and inside layers, the combined PDOS of all Co atoms from each layer of (100) slab and (111) Co/Cu slab have been plotted and presented in Figure 8. In this case, the layer 0 refers to the surface layer, while the deeper layers are denoted as layer 1, layer 2 and layer 3 (center). Notably, in Figure 8 (a), the surface layer shows a much unique DOS compared with that of the inside layers in the (100) slab. The DOS of the top layer is less intense near the Fermi level while it is likely to be increased for the deeper layers. The origin of energy shift for the surface states is possibly due to the stronger magnetic exchange interactions that split these Co *d*-states apart. The magnetic moment on Co, given in Table S4, decreases from layer 0 (2.10 μ_B) to layer 3 (0.78 μ_B) – in accord with shorter Co-Se bond distances and stronger bond distortion for the surface layer, also listed in Table S4. Thus, the central layer in the (100) slab resembles the electronic and magnetic properties of bulk $CuCo_2Se_4$. In contrast, there is no apparent correlation between the Co magnetic moment and the layer depth in the (111) slab: the top layer 0 has the highest magnetic moment (2.29 μ_B), similar to the (100) case, however, the following layer 1 has the lowest magnetic moment (1.47 μ_B) and the magnetic moment is large in the layers 2 and 3 (~2.1 μ_B), more than double of that in the bulk value (0.79 μ_B). Therefore, the structural reconstruction and surface enhancement of the magnetic properties of Co atoms is much deeper for the slab with (111) surface orientation than that for the (100) slab where only the top surface layer is affected. It should be noted here that in

contrast to (100) slab with similar metal composition of the layers, in the (111) slab, the layer 1 and layer 3 consist of only Co atoms while both Co and Cu atoms are present in the layer 0 and layer 2. The Co atoms in layer 0 has Co-Se bond distance of 2.23 Å which is the shortest one in comparison to that found in bulk $CuCo_2Se_4$ (2.40 Å). As a result, both the spin up and spin down states are narrower for Co atom in the surface layer as compared to deeper layers, (Figure 8 (b)), however, the Co atom in the top layer has spin down CB states closest to the Fermi level (at ~1 eV). These states participate in OH^- adsorption, as shown below.

To investigate which metal atom on the surface is more likely to be the catalytically active site for OER, the adsorption of OH^- on (100) and (111) Co/Cu terminated slabs was modeled by placing OH^- ion in the vicinity of the active metal site (Co or Cu) of the relaxed free surface at an initial distance of about 2.2 Å from the metal atom. The GGA+U total energy of the fully-optimized structure with OH^- bonded to the surface Co atom is 0.53 eV and 2.03 eV higher than that bonded to the Cu atom for the (100) and (111) surface, respectively. The large energy difference, especially in the (111) case, suggests that Co atom is the highly preferred catalytically active site. We should note here that the energy difference between the adsorption of OH^- on Co

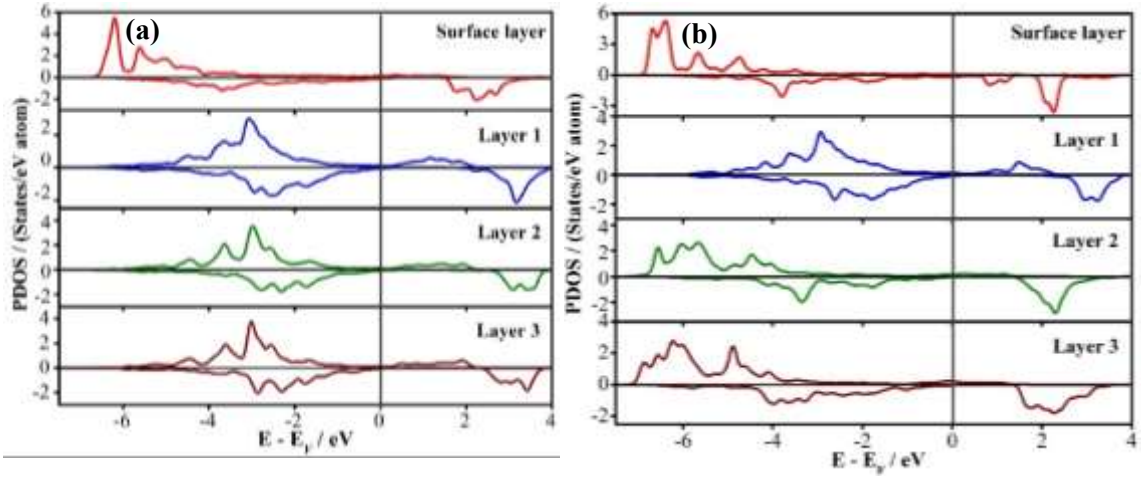

Figure 8. Combined partial density of states (PDOS) of all Co atoms in each layer for (100) slab (a) and (111) Co/Cu terminated slab (b).

vs Cu is much smaller within GGA (U=0 eV), namely, 0.04 eV and 0.52 eV for the (100) and (111) case, respectively, suggesting that magnetism plays a crucial role in favoring the OH^- adsorption on Co. The comparison of PDOS of Co and Cu atoms with and without OH^- attachment is shown in Figure 9 and Figure S15, respectively. For both Co and Cu with OH^- ion attached, there is a significant orbital splitting of the occupied metal states associated with rearranged electron cloud. In addition, in all cases except for Cu-OH at (111) surface, a strong hybridization of the metal states with the states of OH^- ion leads to a more intense density of states in the VB near the Fermi level as compared to OH^--free surfaces. Further, comparing energetics of the OH^- ion bonded to Co on (100) *vs* (111) surface, we find that the OH^- adsorption on the (111) Co/Cu terminated surface is energetically more favorable by as much as 7 eV as shown in Table S5. While the Co-O distances or Co-O-H angles are relatively similar for the (100) and (111) slabs, namely, 1.81 Å and 1.76 Å or 110.4^o and 123.1^o, respectively, we believe that the huge energy difference for OH^- ion adsorption on Co at two different surface orientations is due to the fact that the Co atom at the (111) surface is 3-coordinated with Se atoms, whereas it is 5-coordinated at the (100) surface. Upon bonding to the OH anion, local magnetic moment on the Co atom increases from 2.1 μ_B to 2.6 μ_B for (100) slab and from to 2.3 μ_B to 2.4 μ_B for (111) slab with Co/Cu termination, whereas the Co-Se distances increase from 2.33 Å to 2.45 Å and from 2.23 Å to 2.30 Å, respectively. Accordingly, the calculated PDOS of Co, (Figure 9), shows that the occupied spin-up Co states become more localized upon bonding with OH^- due to the weaker Co-Se interactions and are shifted to the lower negative energy because of the stronger magnetic exchange splitting. On the other hand, the PDOS exhibit opposite trends in the empty spin-down states of Co for (100) and (111) slabs, namely, the shift to the lower and higher energy, respectively, as shown in Figure 9. Finally, we aligned the DOS of the (100) and (111) Co/Cu terminated slabs with OH^- ion attached

to Co atom on each surface with respect to the semi-core O-2*s* states and observed that the Fermi level of the (111) surface is about 0.2-0.3 eV lower as compared to that of the (100) surface – in accord with the preferred OH^- adsorption on the (111) surface orientation of $CuCo_2Se_4$.

From the DFT studies of the electronic properties and the OH^- adsorption calculations on the different surfaces of $CuCo_2Se_4$, it can be concluded that Co atom is the active catalytic site for the $CuCo_2Se_4$ system. However, the presence of Cu on the neighboring sites influences the electronic density around the Co ions as well as its magnetic moment. Specifically, the alternate Co-only and Cu/Co layers in the slab with (111) surface orientation (Figure 6), results in significant variance of the layer-dependent magnetic moment of Co and, hence, its electronic properties, making surface enhancement of the magnetic interactions penetrate deeper into the (111) slab and leading to OH^- adsorption being energetically favorable on the (111) surface. Furthermore, in cobalt based materials, Co^{3+} has been widely accepted as the effective catalytic active site resulting in $Co^{2+} \rightarrow Co^{3+}$ redox conversion during the OER process.[67] The $Co^{2+} \rightarrow Co^{3+}$ oxidation is visible as a peak at around 1.1 V (vs RHE) in the OER LSV, which is consistent with the data shown in Figure

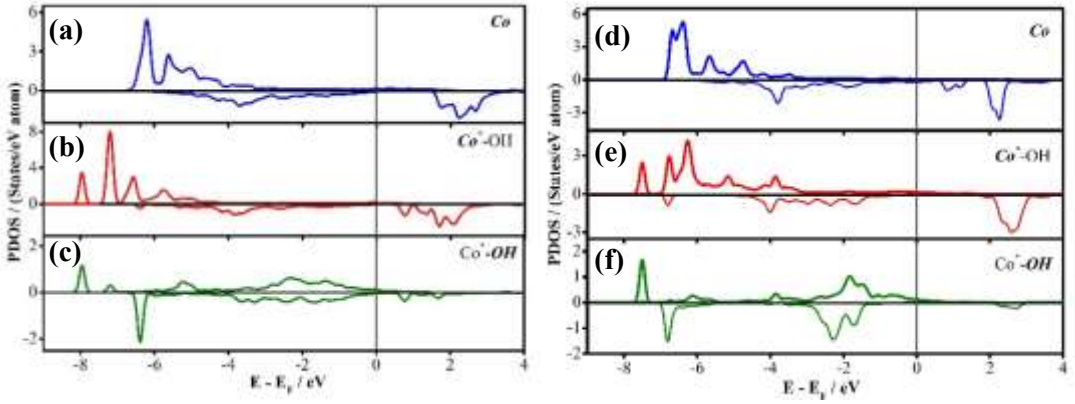

Figure 9. Partial density of states (PDOS) of Co atom in (100) surface before OH^- attachment (a), Co atom after OH^- attachment (b), OH^- ions after attachment on Co atom (c). PDOS of Co atom in (111) surface before OH^- attachment (d), Co atom after OH^- attachment (e), OH^- ions after attachment on Co atom (f).

2. Such catalyst activation will be enhanced as the presence of Cu redistributes the electron density around Co through *d-d* interactions as was also observed in the DFT studies. The increased amount of Co^{3+} seen in XPS also confirms that Co sites are more likely to serve as the active catalytic site for OER. Specifically, in catalysts with spinel structure, metal ions occupying the octahedral sites has been observed to be more active for OER.[70] The availability of additional sites for OH^- adsorption on Cu will also possibly increase hydrophilicity of the surface leading to better wettability and improved catalytic performance. The inclusion of Cu also enhances metallic states and electrical conductivity within the composite.

Conclusions

In summary, $CuCo_2Se_4$ has been reported for the first time as a bifunctional electrocatalyst for overall water splitting. The OER and HER electrocatalytic property was studied through detailed electrochemical measurements which revealed that the catalyst required a low overpotential of 320 mV and 232 mV to achieve 50 mA cm^{-2} for OER and HER, respectively, and exhibited promising durability in alkaline solution. The overpotential for OER was significantly lower than that of RuO_2 and was amongst the lowest for selenide based OER electrocatalysts. A comparison with the other reported Co and/or Cu-based OER/HER catalyst (Table S6) revealed that $CuCo_2Se_4$ presented in this paper is even better than the best Cu and/or Co-based OER catalyst. Importantly, the catalyst can be applied for full water splitting and can achieve a current density of 50 mA cm^{-2} at a cell voltage of 1.782 V with energy efficiency of 83.05 %. The $CuCo_2Se_4$ nanostructure synthesized through one-step hydrothermal method provides a new composition of high-efficiency electrocatalysts comprising economical and earth abundant transition metals. First-principles electronic structure calculations of bulk and (100) and (111) lattice plane terminated slabs of $CuCo_2Se_4$ as well as comparison of OH^- adsorption energies on the corresponding surfaces provided significant insight into the origin of observed catalytic performance and possible

catalytically active sites in this material. Based on the extensive DFT calculations, it was concluded that Co is the actual catalytically active site in this material. However, the presence of neighboring Cu atoms enhances catalytic activity on the Co site through electron redistribution, as well as enhancement of the local magnetic moment which effects OH^- adsorption energy on the catalytic site, leading to faster onset of OER and reduction of overpotential. Such knowledge regarding the effect of transition metal doping on the OER catalytic activity as well the positive effect of presence of Cu near the catalytic site, can be extended to design other OER catalytic system with predictively high efficiencies.

ASSOCIATED CONTENT

Supporting Information. Procedure of electrodeposition of RuO_2, ECSA, OER LSV comparison plots, zoomed-in OER LSV plot, zoomed-in HER and HER LSV plots, EIS plot and table, SEM comparison before and after stability, XPS comparison before and after stability, LSV plot and table of water electrolyzer, DFT result table, DOS of bulk $CuCo_2Se_4$, PDOS of Cu atoms and OER comparison table.

AUTHOR INFORMATION

Corresponding Author

*Manashi Nath: nathm@mst.edu

Author Contributions

The manuscript was written through contributions of all authors. All authors have given approval to the final version of the manuscript.

Funding Sources

This work was supported by funding from National Science Foundation (DMR 1710313) and American Chemical Society Petroleum Research Fund (54793-ND10). Computational resources were provided by DOE-supported NERSC (*National Energy Research Scientific Computing)* center for high-performance computing.

Notes

Any additional relevant notes should be placed here.

ACKNOWLEDGMENT

The authors would like to acknowledge the funding from National Science Foundation (DMR 1710313) and American Chemical Society Petroleum Research Funds (54793-ND10). The authors would also like to acknowledge Materials Research Center (MRC) for equipment usage. This research used resources of the National Energy Research Scientific Computing Center, a DOE Office of Science User Facility supported by the Office of Science of the U.S. Department of Energy under Contract No. DE-AC02-05CH11231.

REFERENCES

(1) Lewis, N. S. Toward Cost-Effective Solar Energy Use. *Science* **2007**, *315*, 798–801.

(2) Walter, M. G.; Warren, E. L.; Mckone, J. R.; Boettcher, S. W.; Mi, Q.; Santori, E. A.; Lewis, N. S. Solar Water Splitting Cells. *Chem. Rev.*, **2010**, *110*, 6446–6473.

(3) Turner, J. A. Sustainable Hydrogen Production. *Science* **2004**, *305*, 972–974.

(4) Suen, N.-T.; Hung, S.-F.; Quan, Q.; Zhang, N.; Xu, Y.-J.; Chen, H. M. Electrocatalysis for the Oxygen Evolution Reaction: Recent Development and Future Perspectives. *Chem. Soc.*

Rev. **2017**, *46*, 337–365.

(5) Rossmeisl, J.; Logadottir, A.; Nørskov, J. K. Electrolysis of Water on (Oxidized) Metal Surfaces. *Chem. Phys.* **2005**, *319*, 178–184.

(6) Jiao, Y.; Zheng, Y.; Jaroniec, M.; Qiao, S. Z. Design of Electrocatalysts for Oxygen- and Hydrogen-Involving Energy Conversion Reactions. *Chem. Soc. Rev.* **2015**, *44*, 2060–2086.

(7) Chaudhari, N. K.; Jin, H.; Kim, B.; Lee, K. Nanostructured Materials on 3D Nickel Foam as Electrocatalysts for Water Splitting. *Nanoscale* **2017**, *9*, 12231–12247.

(8) Matsumoto, Y.; Sato, E. Electrocatalytic Properties of Transition Metal Oxides for Oxygen Evolution Reaction. *Mater. Chem. Phys.* **1986**, *14*, 397–426.

(9) Mccrory, C. C. L.; Jung, S.; Peters, J. C.; Jaramillo, T. F. Benchmarking Heterogeneous Electrocatalysts for the Oxygen Evolution Reaction. *J. Am. Chem. Soc.* **2013**, *135*, 16977−16987.

(10) Hamann, T. W. Water Splitting: An Adaptive Junction. *Nat. Mater.* **2013**, *13*, 3–4.

(11) Dau, H.; Limberg, C.; Reier, T.; Risch, M.; Roggan, S.; Strasser, P. The Mechanism of Water Oxidation: From Electrolysis via Homogeneous to Biological Catalysis. *ChemCatChem* **2010**, *2*, 724–761.

(12) Roger, I.; Shipman, M. A.; Symes, M. D. Earth-Abundant Catalysts for Electrochemical and Photoelectrochemical Water Splitting. *Nat. Rev. Chem.* **2017**, *1*, 0003.

(13) Gong, M.; Dai, H. A Mini Review of NiFe-Based Materials as Highly Active Oxygen Evolution Reaction Electrocatalysts. *Nano Res.* **2015**, *8*, 23–39.

(14) Geiger, S.; Kasian, O.; Shrestha, B. R.; Mingers, A. M.; Mayrhofer, K. J. J.; Cherevko, S. Activity and Stability of Electrochemically and Thermally Treated Iridium for the Oxygen Evolution Reaction. *J. Electrochem. Soc.* **2016**, *163*, F3132–F3138.

(15) Lee, Y.; Suntivich, J.; May, K. J.; Perry, E. E.; Shao-Horn, Y. Synthesis and Activities of Rutile IrO_2 and RuO_2 Nanoparticles for Oxygen Evolution in Acid and Alkaline Solutions. *J. Phys. Chem. Lett.* **2012**, *3*, 399–404.

(16) Reier, T.; Oezaslan, M.; Strasser, P. Electrocatalytic Oxygen Evolution Reaction (OER) on Ru, Ir, and Pt Catalysts: A Comparative Study of Nanoparticles and Bulk Materials. *ACS Catal.* **2012**, *2*, 1765–1772.

(17) Jiao, F.; Frei, H. Nanostructured Cobalt Oxide Clusters in Mesoporous Silica as Efficient Oxygen-Evolving Catalysts. *Angew. Chem. Int. Ed.* **2009**, *48*, 1841–1844.

(18) Wang, Y.; Xie, C.; Liu, D.; Huang, X.; Huo, J.; Wang, S. Nanoparticle-Stacked Porous Nickel-Iron Nitride Nanosheet: A Highly Efficient Bifunctional Electrocatalyst for Overall Water Splitting. *ACS Appl. Mater. Interfaces* **2016**, *8*, 18652–18657.

(19) Hong, W. T.; Risch, M.; Stoerzinger, K. A.; Grimaud, A.; Suntivich, J.; Shao-Horn, Y. Toward the Rational Design of Non-Precious Transition Metal Oxides for Oxygen Electrocatalysis. *Energy Environ. Sci.* **2015**, *8*, 1404–1427.

(20) Yu, X.-Y.; Feng, Y.; Guan, B.; Lou, X. W.; Paik, U. Carbon Coated Porous Nickel Phosphides Nanoplates for Highly Efficient Oxygen Evolution Reaction. *Energy Environ. Sci.* **2016**, *9*, 1246–1250.

(21) Du, H.; Kong, R. M.; Guo, X.; Qu, F.; Li, J. Recent Progress in Transition Metal Phosphides

with Enhanced Electrocatalysis for Hydrogen Evolution. *Nanoscale* **2018**, *10*, 21617–21624.

(22) Liu, M.; Li, J. Cobalt Phosphide Hollow Polyhedron as Efficient Bifunctional Electrocatalysts for the Evolution Reaction of Hydrogen and Oxygen. *ACS Appl. Mater. Interfaces* **2016**, *8*, 2158–2165.

(23) Landon, J.; Demeter, E.; Inoğlu, N.; Keturakis, C.; Wachs, I. E.; Vasić, R.; Frenkel, A. I.; Kitchin, J. R. Spectroscopic Characterization of Mixed Fe-Ni Oxide Electrocatalysts for the Oxygen Evolution Reaction in Alkaline Electrolytes. *ACS Catal.* **2012**, *2*, 1793–1801.

(24) Burke, M. S.; Enman, L. J.; Batchellor, A. S.; Zou, S.; Boettcher, S. W. Oxygen Evolution Reaction Electrocatalysis on Transition Metal Oxides and (Oxy)Hydroxides: Activity Trends and Design Principles. *Chem. Mater.* **2015**, *27*, 7549–7558.

(25) Yang, Y.; Fei, H.; Ruan, G.; Xiang, C.; Tour, J. M. Efficient Electrocatalytic Oxygen Evolution on Amorphous Nickel-Cobalt Binary Oxide Nanoporous Layers. *ACS Nano* **2014**, *8*, 9518–9523.

(26) Anantharaj, S.; Kennedy, J.; Kundu, S. Microwave-Initiated Facile Formation of Ni_3Se_4 Nanoassemblies for Enhanced and Stable Water Splitting in Neutral and Alkaline Media. *ACS Appl. Mater. Interfaces* **2017**, *9*, 8714–8728.

(27) Wang, Z.; Li, J.; Tian, X.; Wang, X.; Yu, Y.; Owusu, K. A.; He, L.; Mai, L. Porous Nickel-Iron Selenide Nanosheets as Highly Efficient Electrocatalysts for Oxygen Evolution Reaction. *ACS Appl. Mater. Interfaces* **2016**, *8*, 19386–19392.

(28) Anantharaj, S.; Ede, S. R.; Sakthikumar, K.; Karthick, K.; Mishra, S.; Kundu, S. Recent

Trends and Perspectives in Electrochemical Water Splitting with an Emphasis on Sulfide, Selenide, and Phosphide Catalysts of Fe, Co, and Ni: A Review. *ACS Catal*. **2016**, *6*, 8069-8097.

(29) Liu, B.; Zhao, Y. F.; Peng, H. Q.; Zhang, Z. Y.; Sit, C. K.; Yuen, M. F.; Zhang, T. R.; Lee, C. S.; Zhang, W. J. Nickel–Cobalt Diselenide 3D Mesoporous Nanosheet Networks Supported on Ni Foam: An All-PH Highly Efficient Integrated Electrocatalyst for Hydrogen Evolution. *Adv. Mater.* **2017**, *29*, 1606521.

(30) Swesi, A. T.; Masud, J.; Nath, M. Nickel Selenide as a High-Efficiency Catalyst for Oxygen Evolution Reaction. *Energy Environ. Sci.* **2016**, *9*, 1771–1782.

(31) Masud, J.; Swesi, A. T.; Liyanage, W. P. R.; Nath, M. Cobalt Selenide Nanostructures: An Efficient Bifunctional Catalyst with High Current Density at Low Coverage. *ACS Appl. Mater. Interfaces* **2016**, *8*, 17292–17302.

(32) Masud, J.; Liyanage, W. P. R.; Cao, X.; Saxena, A.; Nath, M. Copper Selenides as High-Efficiency Electrocatalysts for Oxygen Evolution Reaction. *ACS Appl. Energy Mater.* **2018**, *1*, 4075–4083.

(33) Swesi, A. T.; Masud, J.; Liyanage, W. P. R.; Umapathi, S.; Bohannan, E.; Medvedeva, J.; Nath, M. Textured $NiSe_2$ Film: Bifunctional Electrocatalyst for Full Water Splitting at Remarkably Low Overpotential with High Energy Efficiency. *Sci. Rep.* **2017**, *7*, 2401.

(34) De Silva, U.; Masud, J.; Zhang, N.; Hong, Y.; Liyanage, W. P. R.; Asle Zaeem, M.; Nath, M. Nickel Telluride as a Bifunctional Electrocatalyst for Efficient Water Splitting in Alkaline Medium. *J. Mater. Chem. A* **2018**, *6*, 7608–7622.

(35) Zhang, G.; Zang, S.; Lan, Z. A.; Huang, C.; Li, G.; Wang, X. Cobalt Selenide: A Versatile Cocatalyst for Photocatalytic Water Oxidation with Visible Light. *J. Mater. Chem. A* **2015**, *3*, 17946–17950.

(36) Xu, K.; Ding, H.; Lv, H.; Tao, S.; Chen, P.; Wu, X.; Chu, W.; Wu, C.; Xie, Y. Understanding Structure-Dependent Catalytic Performance of Nickel Selenides for Electrochemical Water Oxidation. *ACS Catal.* **2017**, *7*, 310–315.

(37) Xu, X.; Song, F.; Hu, X. A Nickel Iron Diselenide-Derived Efficient Oxygen-Evolution Catalyst. *Nat. Commun.* **2016**, *7*, 12324.

(38) Cao, X.; Johnson, E.; Nath, M. Expanding Multinary Selenide Based High-Efficiency Oxygen Evolution Electrocatalysts through Combinatorial Electrodeposition: Case Study with Fe-Cu-Co Selenides. *ACS Sustain. Chem. Eng.* **2019**, *7*, 9588–9600.

(39) Cao, X.; Johnson, E.; Nath, M. Identifying High-Efficiency Oxygen Evolution Electrocatalysts from Co–Ni–Cu Based Selenides through Combinatorial Electrodeposition. *J. Mater. Chem.* **2019**, 7, 9877–9889.

(40) Cao, X.; Hong, Y.; Zhang, N.; Chen, Q.; Masud, J.; Zaeem, M. A.; Nath, M. Phase Exploration and Identification of Multinary Transition-Metal Selenides as High-Efficiency Oxygen Evolution Electrocatalysts through Combinatorial Electrodeposition. *ACS Catal.* **2018**, *8*, 8273–8289.

(41) Hong, W. T.; Welsch, R. E.; Shao-Horn, Y. Descriptors of Oxygen-Evolution Activity for Oxides: A Statistical Evaluation. *J. Phys. Chem. C* **2016**, *120*, 78–86.

(42) Suntivich, J.; May, K. J.; Gasteiger, H. A.; Goodenough, J. B.; Shao-Horn, Y. A Perovskite

Oxide Optimized for Oxygen Evolution Catalysis from Molecular Orbital Principles. *Science* **2011**, *334*, 1383–1385.

(43) Maiyalagan, T.; Jarvis, K. A.; Therese, S.; Ferreira, P. J.; Manthiram, A. Spinel-Type Lithium Cobalt Oxide as a Bifunctional Electrocatalyst for the Oxygen Evolution and Oxygen Reduction Reactions. *Nat. Commun.* **2014**, *5*, 3949.

(44) Liu, Y.; Niu, Z.; Lu, Y.; Zhang, L.; Yan, K. Facile Synthesis of $CuFe_2O_4$ crystals Efficient for Water Oxidation and H_2O_2 reduction. *J. Alloys Compd.* **2018**, *735*, 654–659.

(45) Chen, Z.; Meyer, T. J. Copper(II) Catalysis of Water Oxidation. *Angew. Chem. Int. Ed.* **2013**, *52*, 700–703.

(46) Bikkarolla, S. K.; Papakonstantinou, P. $CuCo_2O_4$ Nanoparticles on Nitrogenated Graphene as Highly Efficient Oxygen Evolution Catalyst. *J. Power Sources* **2015**, *281*, 243–251.

(47) Chauhan, M.; Reddy, K. P.; Gopinath, C. S.; Deka, S. Copper Cobalt Sulfide Nanosheets Realizing a Promising Electrocatalytic Oxygen Evolution Reaction. *ACS Catal.* **2017**, *7*, 5871–5879.

(48) Zhao, Q.; Yan, Z.; Chen, C.; Chen, J. Spinels: Controlled Preparation, Oxygen Reduction/Evolution Reaction Application, and Beyond. *Chem. Rev.* **2017**, *117*, 10121–10211.

(49) Han, X.; He, G.; He, Y.; Zhang, J.; Zheng, X.; Li, L.; Zhong, C.; Hu, W.; Deng, Y.; Ma, T. Y. Engineering Catalytic Active Sites on Cobalt Oxide Surface for Enhanced Oxygen Electrocatalysis. *Adv. Energy Mater.* **2018**, *8*, 1702222.

(50) Kresse, G.; Hafner, J. Ab Initio Molecular Dynamics for Liquid Metals. *Phys. Rev. B* **1993**,

47, 558–561.

(51) Kresse, G.; Hafner, J. Ab Initio Molecular-Dynamics Simulation of the Liquid-Metal–amorphous-Semiconductor Transition in Germanium. *Phys. Rev. B* **1994**, *49*, 14251–14269.

(52) Kresse, G.; Furthmüller, J. Efficient Iterative Schemes for Ab Initio Total-Energy Calculations Using a Plane-Wave Basis Set. *Phys. Rev. B* **1996**, *54*, 11169–11186.

(53) Kresse, G.; Furthmüller, J. Efficiency of Ab-Initio Total Energy Calculations for Metals and Semiconductors Using a Plane-Wave Basis Set. *Comput. Mater. Sci.* **1996**, *6*, 15–50.

(54) Perdew, J. P.; Burke, K.; Ernzerhof, M. Generalized Gradient Approximation Made Simple. *Phys. Rev. Lett.* **1996**, *77*, 3865–3868. Erratum: Generalized Gradient Approximation Made Simple. *Phys. Rev. Lett.* **1997**, *78*, 1396–1396.

(55) Blöchl, P. E. Projector Augmented-Wave Method. *Phys. Rev. B* **1994**, *50*, 17953–17979.

(56) Kresse, G; Joubert, D. From Ultrasoft Pseudopotentials to the Projector Augmented-Wave Method. *Phys. Rev. B* **1999**, *59*, 1758–1775.

(57) Philipsen, P. H. T.; Baerends, E. J. Cohesive Energy of 3d Transition Metals: Density Functional Theory Atomic and Bulk Calculations. *Phys. Rev. B* **1996**, *54*, 5326–5333.

(58) Kohn, W.; Becke, A. D.; Parr, R. G. Density Functional Theory of Electronic Structure. *J. Phys. Chem.* **1996**, *100*, 12974–12980.

(59) Dudarev, S.; Botton, G. Electron-Energy-Loss Spectra and the Structural Stability of Nickel Oxide: An LSDA+U Study. *Phys. Rev. B* **1998**, *57*, 1505–1509.

(60) Holzwarth, U.; Gibson, N. The Scherrer Equation versus the 'Debye-Scherrer Equation'. *Nat.*

Nanotechnol. **2011**, *6*, 534.

(61) Chen, H.; Chen, S.; Fan, M.; Li, C.; Chen, D.; Tian, G.; Shu, K.; Walsh, F. C.; Zhu, J.; Chen, M. Bimetallic Nickel Cobalt Selenides: A New Kind of Electroactive Material for High-Power Energy Storage. *J. Mater. Chem. A* **2015**, *3*, 23653–23659.

(62) Kim, K. M.; Nam, J. H.; Lee, Y. G.; Cho, W. Il; Ko, J. M. Supercapacitive Properties of Electrodeposited RuO_2 Electrode in Acrylic Gel Polymer Electrolytes. *Curr. Appl. Phys.* **2013**, *13*, 1702–1706.

(63) Xiao, P.; Sk, M. A.; Thia, L.; Ge, X.; Lim, R. J.; Wang, J. Y.; Lim, K. H.; Wang, X. Molybdenum Phosphide as an Efficient Electrocatalyst for the Hydrogen Evolution Reaction. *Energy Environ. Sci.* **2014**, *7*, 2624–2629.

(64) Sheng, W.; Gasteiger, H. A.; Shao-Horn, Y. Hydrogen Oxidation and Evolution Reaction Kinetics on Platinum: Acid vs Alkaline Electrolytes. *J. Electrochem. Soc.* **2010**, *157*, B1529–B1536.

(65) Momma, K.; Izumi, F. VESTA 3 for Three-Dimensional Visualization of Crystal, Volumetric and Morphology Data. *J. Appl. Crystallogr.* **2011**, *44*, 1272–1276.

(66) Friebel, D.; Louie, M. W.; Bajdich, M.; Sanwald, K. E.; Cai, Y.; Wise, A. M.; Cheng, M. J.; Sokaras, D.; Weng, T. C.; Alonso-Mori, R. Identification of Highly Active Fe Sites in (Ni,Fe)OOH for Electrocatalytic Water Splitting. *J. Am. Chem. Soc.* **2015**, *137*, 1305–1313.

(67) Burke, M. S.; Kast, M. G.; Trotochaud, L.; Smith, A. M.; Boettcher, S. W. Cobalt-Iron (Oxy)Hydroxide Oxygen Evolution Electrocatalysts: The Role of Structure and Composition on Activity, Stability, and Mechanism. *J. Am. Chem. Soc.* **2015**, *137*,

3638−3648.

(68) Ohzuku, H.; Ikeno, H.; Yamada, I.; Yagi, S. First-Principles Calculations of the OH− Adsorption Energy on Perovskite Oxide. *AIP Conference Proceedings*n **2016**, *1763*, 040005.

(69) Su, D.; Dou, S.; Wang, G. Single Crystalline Co_3O_4 Nanocrystals Exposed with Different Crystal Planes for Li-O_2 Batteries. *Sci. Rep.* **2015**, *4*, 5767.

(70) Liu, Q.; Chen, Z.; Yan, Z.; Wang, Y.; Wang, E.; Wang, S.; Wang, S.; Sun, G. Crystal-Plane-Dependent Activity of Spinel Co_3O_4 Towards Water Splitting and the Oxygen Reduction Reaction. *ChemElectroChem* **2018**, *5*, 1080–1086.

Table of Contents Graphic